Check for updates

MATERIALS SCIENCE

Pixelation of perovskite quantum wire thin films with 0.18-µm features and 63,500-ppi pixel density

Qianpeng Zhang^{1,2}*†, Xiaofei Sun²†, Guanyu Chen¹†, Zichao Ma²‡, Daquan Zhang², Yu Zhou², Xiao Qiu², Beitao Ren², Yucheng Ding², Swapnadeep Poddar², Wenying Tang², Hualiang Lv¹*, Xiaoliang Mo¹*, Zhiyong Fan^{2,3}*

Halide perovskite materials excel in broad optoelectronic applications, and there is an urgent demand to develop perovskite-based integrated optoelectronic devices. However, the limitations posed by the incompatibility of perovskite thin film with wet lithography greatly hinder its potential in many important applications, including ultrahigh-density displays, high-resolution image sensors, high-density memristors, and integrated photonic circuitry. To tackle this bottleneck problem, we develop the self-aligned close-spaced sublimation growth of perovskite quantum wires and demonstrate 0.18-micrometer feature size perovskite patterns, meanwhile achieving a pixel density of 63,500 pixels per inch, the highest reported for perovskite. We showcase pixelation of perovskite quantum wires with color conversion films, addressing the need for full-color microdisplays. In addition, we demonstrate these films on curved substrates, holding promise for near-eye microdisplays. Processes shown here can also apply to other perovskite devices such as high-resolution displays, image sensing, and memristor arrays.

Copyright © 2025 The Authors, some rights reserved; exclusive licensee American Association for the Advancement of Science. No claim to original U.S.
Government Works.
Distributed under a Creative Commons Attribution
NonCommercial
License 4.0 (CC BY-NC).

INTRODUCTION

Over the past decade, the development of perovskite optoelectronic devices has been extremely exciting (1). Various types of perovskite devices, such as photovoltaics (2), photodetectors (3), light-emitting diodes (LEDs) (4), and others (5, 6) have achieved numerous performance breakthroughs. However, these studies have primarily focused on enhancing the performance of individual devices. Compared to traditional semiconductor devices, there remains a huge gap in achieving large-scale device integration using halide perovskites. A core barrier to the large-scale, high-density integration of perovskite optoelectronic devices is the incompatibility of perovskite materials with wet lithography processes. Taking micro-LED research as an example, GaN micro-LEDs can achieve pixel sizes as small as 3 µm (7), whereas perovskite materials are still limited to pixelation at the sub-10-μm level. As discussed by a few works, the ionic nature of perovskite materials makes them easily soluble in common polar solvents (8), and high-intensity ultraviolet (UV) light is also harmful to perovskite materials (9). Even with some indirect lithography techniques (8-10), achieving smaller pixel sizes remains a challenge. For example, in recent research by Zhong and colleagues (9), perovskite quantum dot precursors were included in photoresist, achieving a maximum pixel density of 2450 pixels per inch (ppi) with a corresponding spacing of 10 µm. Another interesting study by Qiu and colleagues (11) involved direct lithography on glass containing perovskite nanocrystals. Moreover, Duan et al. (12) reported a perovskite pixel

feature size of 1 μ m using a programmable mixed electrohydrodynamic printing technique. As summarized by Choi and coworkers (13), the minimum pattern sizes of perovskites achieved with photolithography, e-beam/laser ablation, inkjet printing/E-jet, thermal evaporation, and transfer printing are 5 μ m, 0.5 μ m, 1 μ m, 20 μ m, and 400 nm, respectively. Despite these advancements, there is a pressing need for a revolutionary pixelization strategy to achieve higher pixel densities for the next generation of high-quality microdisplays. Only by resolving this critical issue can we make breakthroughs in high-resolution image detection (14), high-density displays (15, 16), and applications such as on-chip optical interconnects and optical communications (17).

Excitingly, our previous work has demonstrated that embedding perovskite materials in porous alumina membranes (PAMs) can yield quantum wires with high stability and high photoluminescence (PL) quantum yield (PLQY) (18). Here, on the basis of perovskite quantum wires in PAM, we have further developed a unique pixelation strategy to explore the downsizing limit of perovskite luminescent pixel. Specifically, the smallest pixel size achieved in this work is 0.18 µm (which is also demonstrated in our Milky Way Galaxy figure). To the best of our knowledge, this is the smallest pixelated perovskite array reported to date. Meanwhile, the highest display density of ~63,500 ppi has also been achieved using square arrays of circular patterns. Furthermore, the most immediate application of ultrahighdensity pixelation is the use of color conversion films for full-color microdisplays. Referring to a recent study on the efficient realization of high-density microdisplay transfer (19), it has been noted that future full-color implementations will require color conversion materials. Considering the latest advancements in microdisplays industries, the most feasible path for achieving full-color displays is through color conversion films. In sync with this idea, here, we have developed red, green, and blue color conversion films using perovskite quantum wire materials. We have also demonstrated ultrahigh-density pixel arrays with pitches of down to 400 nm. Given that state-of-the-art micro-LEDs currently achieve pixel sizes of 3 µm, corresponding to a pixel density of about 8000 ppi (7), our pixelated perovskite arrays hold tremendous potential in serving as promising candidates as color conversion materials. Furthermore, we have also applied these color

¹State Key Laboratory of Photovoltaic Science and Technology, Shanghai Frontiers Science Research Base of Intelligent Optoelectronics and Perception, Institute of Optoelectronics, Fudan University, Shanghai 200433, China. ²Department of Electronic and Computer Engineering, State Key Laboratory of Advanced Displays and Optoelectronics Technologies, The Hong Kong University of Science and Technology, Clear Water Bay, Kowloon, Hong Kong SAR, China. ³Department of Chemical and Biological Engineering, The Hong Kong University of Science and Technology, Clear Water Bay, Kowloon, Hong Kong SAR 999077 China.

^{*}Corresponding author. Email: eezfan@ust.hk (Z.F.); zhang_qp@fudan.edu.cn (Q.Z.); lv_hl@fudan.edu.cn (H.L.); xlmo@fudan.edu.cn (X.M.)

[†]These authors contribute equally to this work.

[‡]Present address: School of Microelectronics, South China University of Technology, Guangzhou 511442, China.

conversion materials to hemispherical transparent substrates resembling contact lenses, paving the way for the development of near-eye contact lens displays in the future. The method shown here is an enabling technology that leads perovskite to wide applications in ultrahigh-density display, high-resolution image sensing, high-density memristors, and integrated photonic circuitry.

RESULTS

In this work, we use several techniques to achieve high-resolution pixelation of perovskite materials. The main idea is to first pattern the PAM template to form a porous surface at the pixel regions while covering or removing the porous material in the spacing regions. Then, perovskite growth is confined to the pixel regions using the self-aligned growth of perovskite quantum wires. Figure 1 depicts the process of self-aligned close-spaced sublimation (sa-CSS) growth of perovskite quantum wires and the different processes involved in

pixelation. In Fig. 1A, the sa-CSS process is illustrated. Perovskite quantum wires selectively grow within the nanopores of the PAM in the pixel region, while the bare fluorine-doped tin oxide (FTO) surface in the spacing region remains free of growth. The CSS growth is achieved by mixing CsPbBr₃ powder, obtained from a 3:1 molar ratio of cesium bromide (CsBr) and lead bromide (PbBr₂). (Note that we chose the inorganic perovskite because it is generally more stable than the organic ones. Moreover, CsPbBr₃ is capable of producing bright-green emission, which is desirable for our application.) The growth process takes place in a quartz tube at a temperature of 400°C and a pressure of 9×10^{-3} torr. In Fig. 1B, the pixelation process is demonstrated using photolithography and reactive ion etching (RIE). Initially, a photoresist is applied and patterned in the pixel region through the photolithography process. Subsequently, the unwanted PAM in the spacing region is selectively removed using RIE. Following this, the perovskite quantum wires are grown within the pixel region using the sa-CSS method to fill the designated area. To achieve ultrahigh

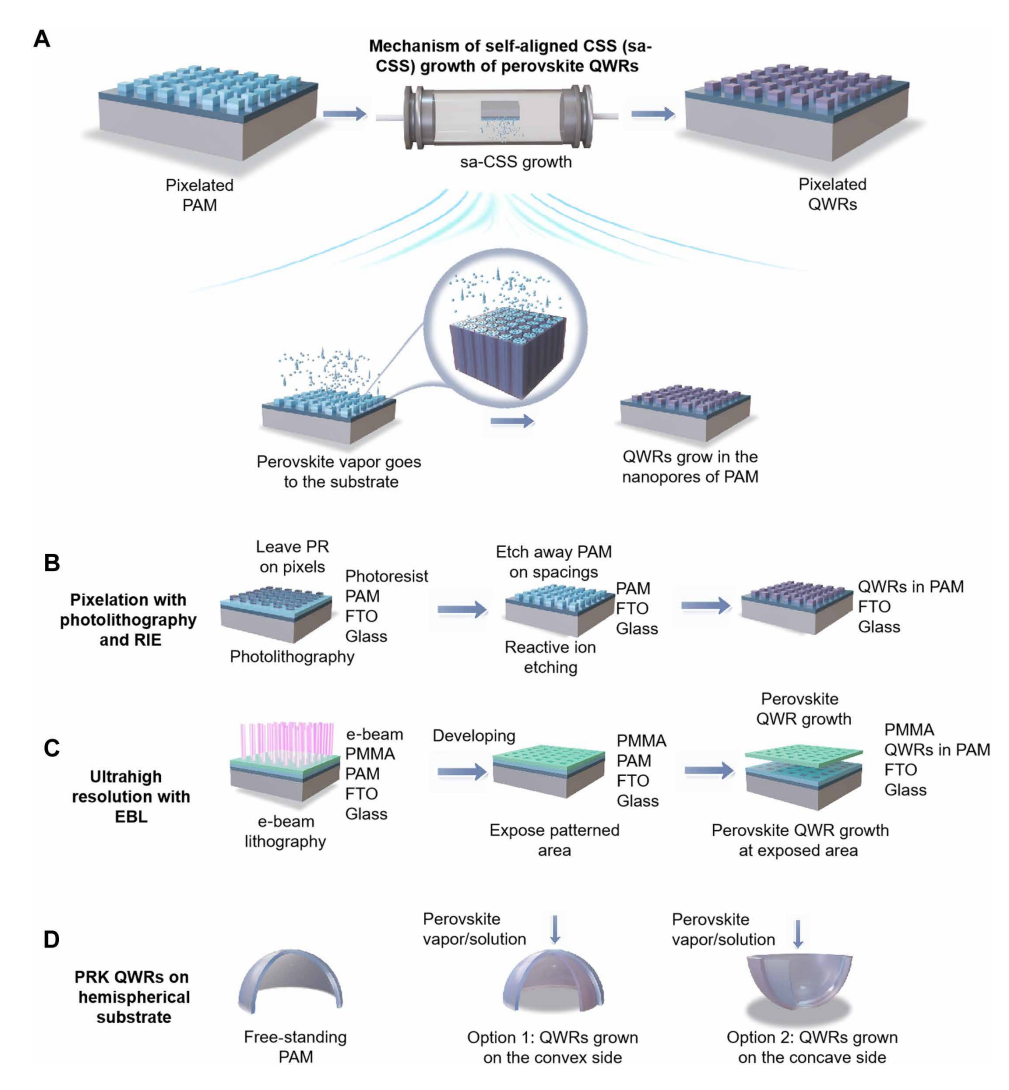


Fig. 1. Mechanism of sa-CSS growth of perovskite quantum wires and different pixelation processes. (A) Mechanism diagram of the sa-CSS method. The PAM enables self-aligned growth in specific areas. (B) Diagram of the pixelation process flow using photolithography and RIE. (C) Diagram of the pixelation process flow using EBL for ultrahigh resolution. The PMMA layer is lifted up in the image to show the quantum wires (QWRs) in the PAM but is not necessarily removed during the experiment. (D) Diagram of the perovskite (PRK) quantum wire growth process flow on nonplanar (e.g., hemispherical) substrate. Quantum wires can grow on either the convex side (option 1) or the concave side (option 2).

resolution and further reduce the pixel size, we incorporated e-beam lithography (EBL) into the process. In this additional step, the pixel region is exposed using EBL, while the spacing region is protected by a layer of polymethyl methacrylate (PMMA). Subsequently, CSS is carried out to selectively grow perovskite quantum wires within the pixel region, as illustrated in Fig. 1C. In Fig. 1C, the PMMA in the image is lifted up in the schematic to show the quantum wires beneath the PAM layer; however, in the actual experiment, the PMMA layer removal process is not required. Figure 1D showcases the process of growing perovskite quantum wires on a hemispherical substrate. The growth of quantum wires can be achieved using either the solution method or the CSS method. In addition, quantum wires can be grown on either the convex side (option 1) or the concave side (option 2) of the substrate.

To understand the underlying mechanisms of the sa-CSS process, we conduct studies using both first-principles theory and molecular dynamics methods, with the findings detailed in Fig. 2. We use first-principles calculations to simulate the adsorption of CsPbBr₃ on the aluminum oxide (Al₂O₃) surface (Fig. 2A), specifically examining the absorption energy at various adsorption sites (table in Fig. 2B). Our results indicate that the Pb—O site exhibits the

lowest energy $(-2.24 \, eV)$ and is, therefore, the most thermodynamically favorable for adsorption. Consequently, the initial phase of the CsPbBr₃ adsorption process on Al₂O₃ predominantly involves the bonding between Pb and O.

To specifically compare the adsorption of CsPbBr₃ gas molecules on different aperture PAMs and planar Al₂O₃ surfaces, we count the number of Pb atoms and O atoms along the transverse direction (X direction) and calculate the number of Pb atoms per unit distance (Fig. 2C). (For PAM, we only calculate the Pb atoms within the pores, while for the flat control, we count all the Pb atoms across the entire simulation area.) It is evident that as the aperture increases, the number of Pb atoms per unit distance also monotonically decreases. When the diameter is 2.6 nm, the number of Pb atoms per unit distance is 69 atoms/nm, whereas when the aperture increases to 13 nm, the number decreases to 23 atoms/nm, which is close to the 18 atoms/nm on the planar Al₂O₃ surface. From our previous discussion, the adsorption of CsPbBr3 gas molecules starts with the binding at the Pb—O sites; therefore, the number of Pb atoms per unit distance to some extent reflects the adsorption capacity of CsPbBr₃ gas molecules in both the porous and planar scenarios. This pattern suggests that, with a fixed amount of injected CsPbBr₃ gas

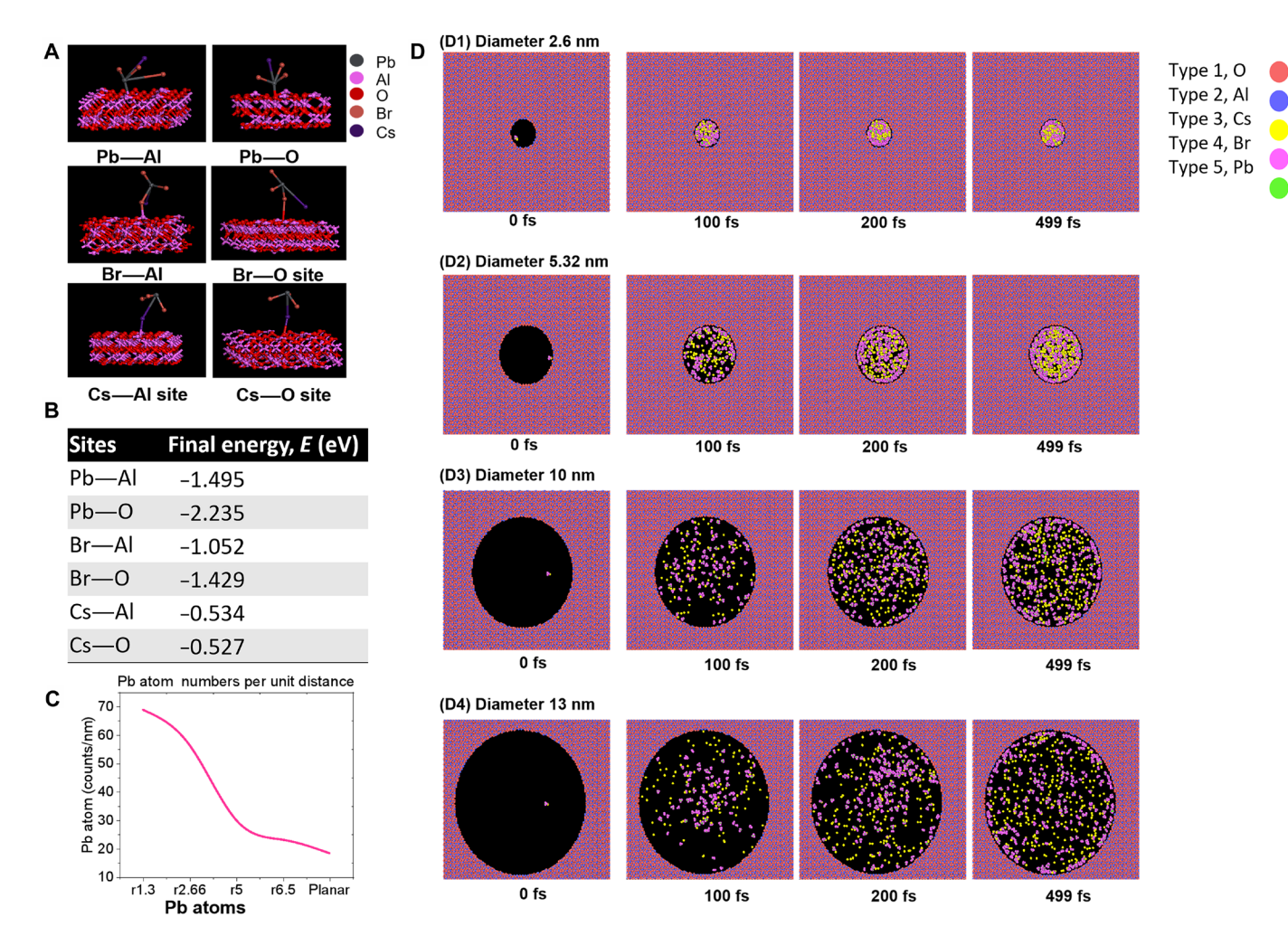


Fig. 2. Mechanisms for sa-CSS growth of perovskite quantum wires and the calculation results from first-principles theory and molecular dynamics method. (A) Adsorption of CsPbBr₃ on the Al_2O_3 surface and the (B) absorption energy at different adsorption sites (results from first-principles theory calculations). (C) Pb atom counts per unit distance for different pore sizes. (D) Adsorption processes of CsPbBr₃ with varying pore sizes (results from molecular dynamics method calculations).

molecules, CsPbBr₃ molecules in smaller pores are more likely to adsorb onto the walls of the alumina tubes, gradually filling these spaces.

Furthermore, we analyze the adsorption behavior of $CsPbBr_3$ gas molecules in PAMs with varying pore sizes and on planar controls. The results (Fig. 2D) show that smaller pores substantially enhance the probability of perovskite gas molecules adsorbing and filling the pores. Conversely, as the pore size increases, the likelihood of $CsPbBr_3$ molecules adsorbing onto the pore walls or previously deposited perovskite decreases.

In contrast, for planar FTO substrates, which effectively have an infinite pore size compared to PAM, the chances of CsPbBr₃ gas molecules adsorbing on the FTO surface are markedly lower than those within the pores of PAM. This differential adsorption behavior is crucial for achieving selective growth and high-density pixelization in our processes.

Observations from Fig. 2 (D1 to D4) reveal that by the end of the simulation (499 fs), pores with diameters of 2.6 and 5.32 nm are substantially filled and show notable growth of perovskite materials. However, the larger pores, with diameters of 10 and 13 nm, do not exhibit substantial filling by the end of the simulation.

Our computational approach uses the Lennard-Jones (LJ) model to describe the intermolecular forces during molecular adsorption at a specific temperature. These forces depend on the relative molecular mass, distance, and interaction strength. In smaller pores, there is a higher frequency of contact and collisions between Pb atoms from CsPbBr₃ and oxygen in alumina, leading to longer durations within bonding ranges and an increased likelihood for bond formation. This initial adsorption facilitates further bonding of subsequent CsPbBr₃ molecules to these sites, culminating in the axial growth of nanocrystals along the pores.

Our observations, supported by first-principles calculations, indicate that perovskite formation occurs exclusively within the nanopores of the PAM and not on bare FTO surfaces. This selective growth is primarily due to the initiation of crystal formation at Pb—O bonding sites, where the formation energy is the lowest. As a result, the amount of perovskite that adheres to the FTO surface is expected to remain minimal.

For the utilization of gaseous materials, the experimental setup involves placing the substrate directly on a quartz boat, with only a 1-mm gap separating it from the perovskite powder. The close proximity of the substrate to the quartz boat creates an almost enclosed space, which we believe considerably minimizes the waste of gaseous materials.

After understanding the self-aligned growth of perovskite quantum wires, we apply this method to grow quantum wires with red, green, and blue colors. In this process, we also use the atomic layer deposition (ALD) method to further shrink the pore size of PAM, enabling control over the quantum wire diameters and, consequently, the bandgaps. Figure 3 shows the application of perovskite quantum wires as color

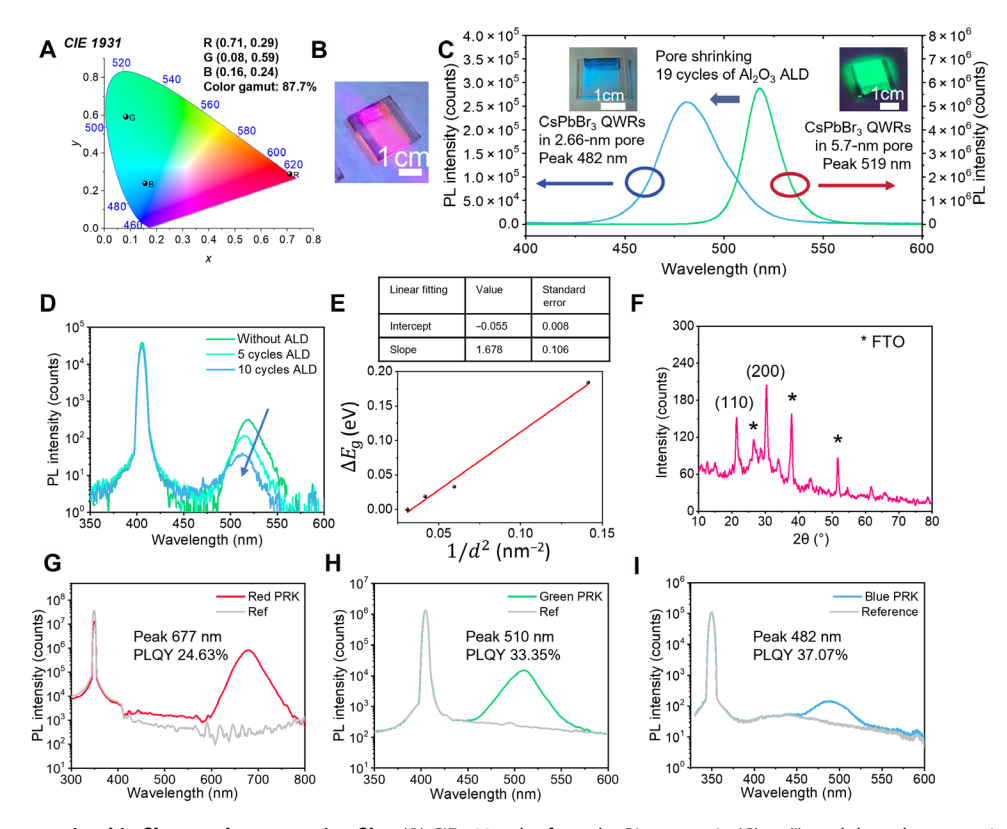


Fig. 3. Perovskite quantum wire thin film as color conversion film. (**A**) CIE 1931 plot from the PL spectra in (G) to (I), and the color gamut is 87.7%. R, red; B, blue; G, green. (**B**) Red color film grown with solution method. (**C**) Change of the film color by controlling the pore size of the PAM. Green and blue films are from $CsPbBr_3$ quantum wires with pore size of 5.7 and 2.66 nm, respectively, giving PL peaks of 519 and 482 nm, respectively. (**D**) PL spectra of $CsPbBr_3$ quantum wires with ALD of 0/5/10 cycles. (**E**) Bandgap shift versus the $1/d^2$, where d is the diameter of the quantum wires. (**F**) XRD spectrum of the $CsPbBr_3$ quantum wires grown in PAM on FTO substrate. (110) and (200) peaks are from perovskite, and peaks marked with asterisk are from SnO_2 . (**G** to **I**) PL spectra of red, green, and blue quantum wire films with excitation light source spectra for PLQY measurement. Emission peaks for red, green, and blue are 677, 510, and 482 nm, respectively, with corresponding PLQYs of 24.63, 33.35, and 37.07%, respectively.

conversion films. Figure 3A is the CIE 1931 plot from the PL spectra, and the color gamut is 87.7%, with red, green, and blue coordinates of (0.71, 0.29), (0.08, 0.59), and (0.16, 0.24) respectively. Figure 3B is the optical photo of a red color quantum wire film under UV light, and the growth is achieved with solution method to have precise component control. The detailed recipe for the red perovskite precursor can be found in Materials and Methods (see the "Red color conversion film" section). Figure 3C is the green and blue quantum wire films acquired from CSS method. Both green and blue films are from the CsPbBr₃ perovskite quantum wires. The major difference is in the pore size control of the PAM, namely, the diameter control of the quantum wires. The green and blue films are composed of quantum wires with a diameter of 5.7 and 2.66 nm, respectively, giving PL peaks of 519 and 482 nm correspondingly. Pore size is reduced by ALD method. ALD conditions can be found in table S1. Figure 3D is the PL spectra of CsPbBr₃ quantum wires with different cycles of Al₂O₃ ALD. A blue shift of the PL peak occurs as the number of ALD cycles increases. On one hand, ALD process reduces the effective area of perovskite materials. On the other hand, according to our previous study (20), the interface between ALD Al₂O₃ and perovskite materials tends to suffer from more defects. As a result, the PL intensity decreases when the pore size shrinks. Figure 3E is the bandgap shift fitting versus $1/d^2$ where d is the diameter of the quantum wires. Detailed emission peaks and bandgap shifts can be found in table S2. Figure 3F is the x-ray diffraction (XRD) pattern of the CsPbBr₃ quantum wires grown in PAM on FTO substrate. Peaks at 21.49° and 30.25° correspond to the (110) and (200) planes of the CsPbBr₃ crystal, respectively. The peaks marked with an asterisk (*) originate from tin oxide (SnO₂). Moreover, we compared the XRD patterns of the samples with and without ALD processes. The XRD spectrum comparison of CsPbBr₃ quantum wires in 5-V PAM with 19 cycles of Al₂O₃ ALD and without ALD is shown in fig. S11. The XRD patterns almost have no change, indicating that the ALD process, which reduces the pore size, does not affect the XRD results. Figure 3 (G to I) is the PLQY spectra for red, green, and blue quantum wire films. PL peaks for red, green, and blue are 677, 510, and 482 nm, respectively. The PLQYs for red, green, and blue are 24.63, 33.35, and 37.07%, respectively.

To investigate the PL behavior of quantum wires/nanowires with larger diameters, we fabricate quantum wires using anodization voltages of 5, 10, 15, and 20 V in PAM and measure their PL. The results are displayed in fig. S8. As the anodization voltage increases, the pore size of the PAM and correspondingly the diameter of the quantum wires also increase. We observe that the PL intensity decreases with an increase in voltage from 5 to 10 and 15 V [quantum wire diameters corresponding to 5.7, 9.1, and 12.2 nm, according to (21)]. The PL intensities for 15 and 20 V (quantum wire diameters corresponding to 12.2 and 18.8 nm) are similar, suggesting that at these higher voltages, the quantum confinement effect is less pronounced.

To test the stability of the quantum wires, we measure the PL degradation for 7 days. The result is as follows. Figure S12 is the PL test under 25°C temperature and 30% relative humidity condition. The samples show almost no degradation in the PL intensities. Furthermore, we measure the PLQYs of green quantum wires with different film thicknesses, and the result is shown in fig. S13. When film thickness increases from 100 to 200 nm, PLQY increases from 32.42 to 53.2%. However, when the thickness further increases to 500 nm, the PLQY drops to 29.53% and remains 30% as the film thickness increases further.

After exploring the patterning method, the mechanism of selfaligned growth, and the growth of differently colored materials, we apply the as-grown quantum wires to a display panel to demonstrate the functionality of the patterned quantum wires. Figure 4 showcases the application of quantum wires for color conversion from a UVA microdisplay panel. The panel is commercially available (from Sitan Limited Company). Specifically, Fig. 4A depicts the perovskite quantum wire arrays, while Fig. 4B illustrates the color conversion demonstration setup. The setup includes a microdisplay panel (UVA) with GaInN micro-LED arrays and drives circuitry at the bottom, a perovskite quantum wire color conversion film in the middle, and a color filter at the top to block unabsorbed backlight. (Blue leakage is related to the thickness of the perovskite quantum wire film. More information can be found in table S3.) Table S3 shows that the film thickness has a critical effect on the light absorption. For quantum wires with 4 nm in diameter and 12.5 nm in pitch, the absorption increases from 3.7 to 91.0%, as film thickness increases from 200 nm to 8 µm. A thicker film will have less blue leakage; however, the anodization of thick Al films sometimes leads to the peeling issues, which requires further optimization on the fabrication processes. Figure 4C shows the UVA image from the display panel, while Fig. 4 (D and E) depicts the same image converted into green and red colors, respectively. Color conversion is achieved using the perovskite quantum wire array, which enables efficient and accurate light conversion from one color to another. The overlapped red and green films are shown in fig. S14. The final image consists of a UVA panel combined with green and red quantum wires, as well as a color filter. Since the green quantum wires are remarkably brighter than the red ones, the overall color closely resembles that of the green quantum wires, albeit with a yellow-green tint. To realize a full color display, both precise alignment of red, green, and blue pixels and pulse-width modulation are required. Overall, Fig. 4 (A to E) provides a comprehensive overview of the color conversion process using quantum wires and highlights the potential of this approach for various display applications.

Because of the well-known stability issues, conventional halide perovskite films prepared by various methods are mostly incompatible with wet lithography approaches, which creates a bottleneck to the use of perovskite materials for integrated optoelectronics. Figure S1 illustrates the comprehensive photolithography process for pixelating perovskite quantum wires, starting with cleaning and preparing the FTO glass substrate, followed by anodization and photolithography to selectively grow perovskite quantum wires, a process critical for creating efficient and precise displays.

Figure 4 (F to K) showcases square pixel arrays based on perovskite quantum wires in red and green, with different pitch sizes. Figure 4 (F to H and I to K) presents square arrays with 10-, 20-, and 30-µm pitch sizes, generated from red and green perovskite quantum wires, respectively. The RIE process removes the alumina in the spacing regions to prevent the growth of perovskite quantum wires, providing a perfect brightness contrast between the spacing and effective parts. Notably, instead of RIE, we also explore the process of covering the spacing PAM with a thick SiO₂ layer to prevent the growth of perovskite quantum wires (fig. S2). However, the SiO₂ layer is not entirely effective at blocking the perovskite vapor, and, thus, the spacing was not completely dark (fig. S3). As a result, we completely remove the alumina from the spacing regions. Overall, Fig. 4 (F to K) provides a valuable visualization of the perovskite quantum wirebased square pixel arrays, with varying pitch sizes and color options.

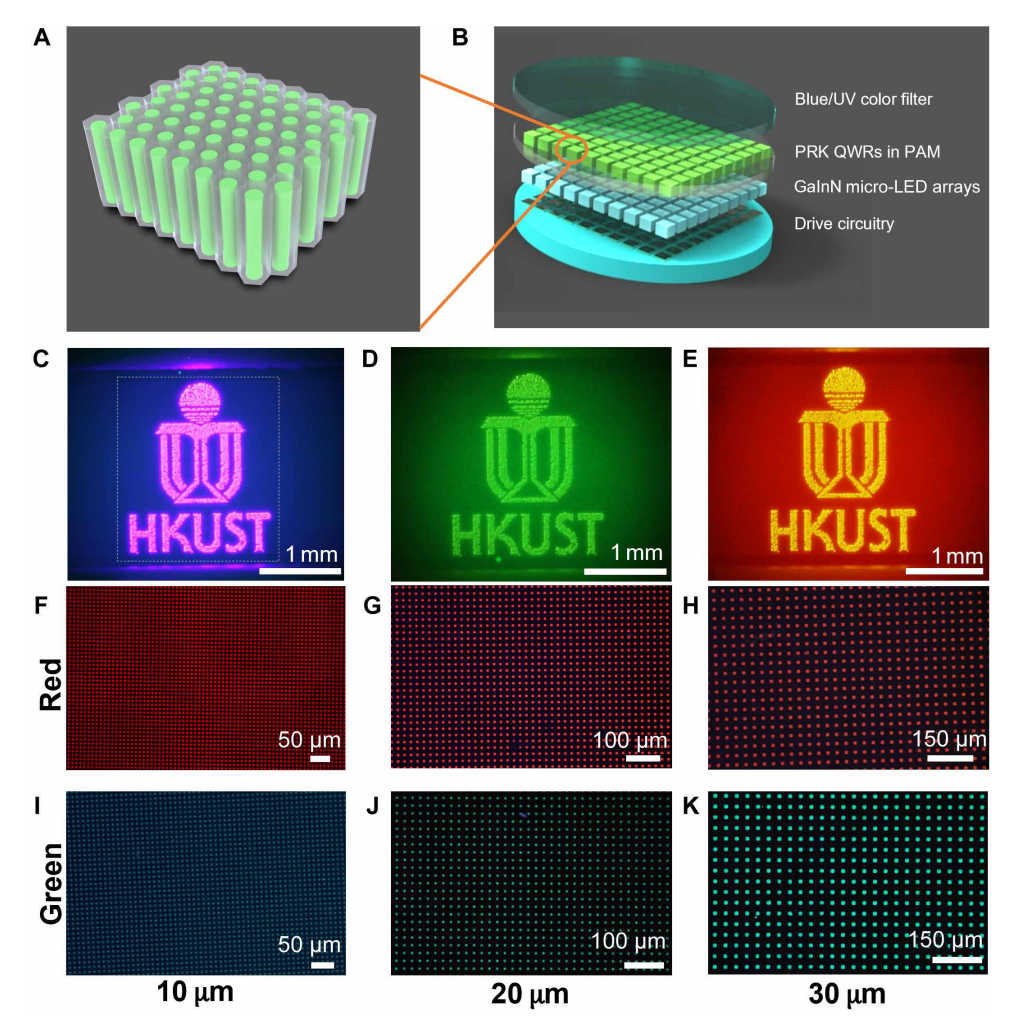


Fig. 4. Demonstration of the color conversion from a UVA microdisplay panel. (A) Diagram of the perovskite quantum wire arrays. (**B**) Diagram of the color conversion demonstration set up. From bottom to top are drive circuitry, GalnN micro-LED arrays, perovskite quantum wires in PAM, and blue/UV color filter. The color filter filters away light with wavelength less than 500 nm. (**C**) UVA panel showing a HKUST logo. The size of the white square dashed lines is 1.95 mm by 1.98 mm. Images converted to (**D**) green and (**E**) red colors. (**F** to **H**) Red and (**I** to **K**) green pixel arrays with pitches of [(F) and (I)] 10 μm, [(G) and (J)] 20 μm, and [(H) and (K)] 30 μm, corresponding to pixel densities of 2540, 1270, and 847 ppi, respectively.

It also highlights the importance of the RIE process in achieving the desired brightness contrast. To enable effective sa-CSS growth, the spacing/nonpixel region should be compact (e.g., FTO itself) rather than a porous material such as SiO₂.

Furthermore, EBL can be used to achieve even smaller feature sizes. Figure S4 demonstrates the process flow for fabricating pixel regions of perovskite quantum wires, starting with the cleaning of FTO glass and culminating in the application of a Ni metal layer and lift-off to expose the pixels, illustrating that perovskites can be successfully integrated into lithography processes with proper protective measures.

To demonstrate the capability of our patterning method, we use the EBL method to achieve an ultrasmall pattern with a pixel size as small as 180 nm and a pitch size of 400 nm. Moreover, we demonstrate patterns of perovskite quantum wires with both ordered arrays and irregular patterns, such as the Milky Way Galaxy. Figure 5 shows the results of pixelation using the process illustrated in fig. S4. EBL is used to achieve smaller feature sizes. Figure 5 (A and B) is

optical and UV photos, respectively, of several quick response (QR) patterns with different sizes. Figure 5 (C and D) shows corresponding images of the red rectangular region in Fig. 5A. The pixel sizes for QR patterns with dimensions of 17 μm by 17 μm , 34 μm by 34 μm , 68 μm by 68 μm , 136 μm by 136 μm , and 272 μm by 272 μm are 0.5, 1, 2, 4, and 8 μm , respectively, as shown in scanning electron microscopy (SEM) images in fig. S5 (A to E). Square arrays of circular patterns with pitch sizes of 0.4, 1, and 4 μm can also be achieved, with SEM images shown in fig. S5 (F to H).

SEM images of the 0.5- μ m pixel-sized QR code (fig. S5A) and the 0.4- μ m pitch-sized square arrays of circular pixels (fig. S5F) are shown. This substantiates that our pixelation process can further enhance the pixel density to 63,500 ppi or even higher. The pixel density depends on the capability of lithography conditions. QR codes here demonstrate the potential for encryption and anticounterfeiting applications by embedding them into art paintings or paper money. In fig. S6, we also show the optical images of the samples during the fabrication process described in fig. S4, including 5- μ m

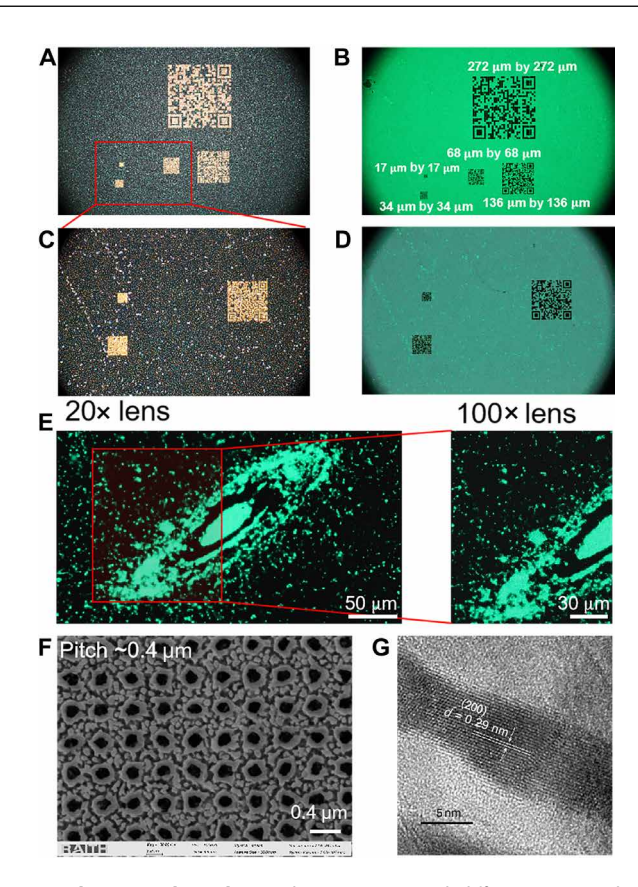


Fig. 5. Pixelation results with EBL. The QR patterns with different sizes are shown. (**A**) Optical photo and (**B**) photo under UV light of QR codes with different sizes: 17 μm by 17 μm, 34 μm by 34 μm, 68 μm by 68 μm, 136 μm by 136 μm, and 272 μm by 272 μm. (**C**) Optical photo and (**D**) photo under UV light of the zoomed-in area indicated with red rectangular in (A). The QR patterns link to the website of our research group. (**E**) Milky Way Galaxy demonstration of the pixelation with feature size down to 0.18 μm. (**F**) SEM image of circular arrays with a pitch size of 400 nm, corresponding to a pixel density of 63,500 ppi. (**G**) Transmission electron microscopy (TEM) image of a single CsPbBr₃ quantum wire.

pitch and 2-µm pitch square arrays, 1-µm distance parallel line arrays, and the clear images of a single QR code.

Our pixelation methods use lithography processes, which are generally considered incompatible with perovskite materials and devices. Therefore, the processes developed in this work demonstrate that our perovskite quantum wires have promising compatibility with lithography in contrast to the conventional planar perovskite films.

With the assistance of high-resolution lithography methods such as EBL, we can obtain pixel patterns with feature size down to 0.18 μm , demonstrated by the Milky Way Galaxy pattern shown in Fig. 5E. The dark regions represent PAM blocked by PMMA, which is the photoresist for EBL, and it shows the flexibility of the sa-CSS growth method. The image shows a clear illustration of the Milky Way Galaxy. The region of the Milky Way Galaxy depicted in our image measures 350 μm by 200 μm , and the size of the stars within it is 0.18 μm . The original image of the Milky Way Galaxy and the corresponding EBL template image can be found in fig. S7. Figure 5F shows the square arrays of circular patterns with the pitch of 400 nm, corresponding to a pixel density of ~63,500 ppi. To the best of our knowledge, no previous work has demonstrated perovskite patterns with such a high pixel density. Figure 5G is the transmission electron microscopy

(TEM) image of a single $CsPbBr_3$ perovskite quantum wire. It shows the (200) planes with a lattice spacing of 2.9 Å, and the diameter of this quantum wire is around 5 nm.

The 0.18- μ m feature-sized pattern was achieved using EBL, which ensures satisfactory location accuracy. Figure 5F also shows the accuracy of the small pixel size. As for the star size in the Milky Way Galaxy pattern, we added SEM characterization, and the result is as follows.

Because the CsPbBr $_3$ quantum wire is grown using high-temperature method, the PMMA material pattern is no longer distinguishable in the SEM image after growth. However, we can still observe the CsPbBr $_3$ crystals corresponding to the pixelated stars. The SEM image is shown in fig. S15A, and the smallest pixel size is even less than 100 nm. Moreover, we also show the sample before perovskite growth (fig. S15B), and the openings in PMMA with a size of 180 nm are clearly visible. The overall image and a zoom-in image of the Milky Way Galaxy PMMA patterns can be found in fig. S16.

Table 1 summarizes some recent reports on perovskite pixelation with different methods and their corresponding feature sizes. Most of the feature sizes reported are still larger than 10 μm . Therefore, the feature size of 180 nm shown in our work provides a substantial advantage over current reports. Moreover, our patterned quantum wires have the advantage of self-passivation due to the alumina template, which blocks water and oxygen invasion and enhances heat dissipation due to the high thermal conductivity of alumina. The complexity of our proposed patterning method lies in applying PAM materials onto semiconductor substrates such as Si; however, this can be resolved by properly sputtering Al onto Si and performing anodization.

Our color conversion film can be shaped into a hemispherical form, making it a potential candidate for curved optoelectronics, such as contact lens microdisplays that could replace current virtual reality/ augmented reality goggles. This is a fundamental device that could serve as an interface to the metaverse. Figure 6 demonstrates the proof of concept of a perovskite quantum wire-based hemispherical color conversion film. Figure 6A shows a diagram of the color conversion film for contact lens microdisplay. Figure 6B displays an optical photo of the freestanding hemispherical semitransparent green color conversion film based on perovskite quantum wires. Note that the sample does not come into contact with human eye and is presented solely for proof-of-concept purposes. Figure 6 (C and D) shows photographs of the convex and concave sides of the green color conversion film under UV light, respectively. Figure 6 (E and F) exhibits photos of the red one. Figure 6G is a diagram of the testing setup for the hemispherical color conversion film. Figure 6H shows the UVA display/color conversion film, and Fig. 6I displays the UVA display/color conversion film/color filter. The bright-green color logo of HKUST is visible. The minimum angular resolution of the human eye is typically 1 arc min. For the contact lens-type neareye displays, the screen is positioned at the surface of the eyeball. Assuming the radius of an adult's eyeball is 12 mm, the calculation is as follows

$$S = 12 \times 10^{-3} \times \frac{\frac{\pi}{180}}{60} \text{m} = 3.49 \times 10^{-6} \text{ m}$$
 (1)

where S is the arc length. Therefore, the human eye can distinguish two objects separated by a distance of 3.49 μ m on the surface of the eyeball, corresponding to 7277 ppi. Thus, our display with 63,500 ppi is completely adequate for this scenario. When the display panel is

Materials	Pixelation method	Applications	Resolution	Feature size	References
Perovskite quantum dots (QDs)/2,5-diphenyloxazole (PPO) and the nonpolar high-refractive index ($n = 1.66$) solvent α -bremnaphthalene	Fill fiber optical template with perovskite QDs	CsPbBr ₃ QDs/PPO liquid scintillator–based x-ray detector	Pore size around 20 μm	20 μm	(24)
Cs _{0.2} FA _{0.8} Pbl _{2.93} Cl _{0.07} perovskite thin film	UV laser scribing	Photodiodes	Minimum pixel size is 70 μm by 130 μm	70 μm	(25)
Cs ₂ AgBiBr ₆ perovskite material	Wafer-scale photolithography	Pixeled perovskite array devices for x-ray detection	Line width of about 10 μm, line spacing of 30 μm	10 μm	(26)
CsPbBr ₃ , CsPbCl ₃ , and CsPbBr _{2.5} l _{0.5} single-crystal fibers	Use fiber arrays	X-ray imaging	Fiber inner diameter of 150 μm	150 μm	(27)
MAPbBr₃ filled in porous Si template	Use Si template	Si-integrated MAPbBr ₃ pillar device for photode- tection	MAPbBr ₃ pillar is approximate- ly in square shape with a side length of ~50 μm	50 μm	(28)
Printed perovskite pixels with graded bandgaps	Inkjet printing	Flexible microspectrom- eters	Square array pitch of about 150 μm, square width of about 80 μm	~80 μm	(29)

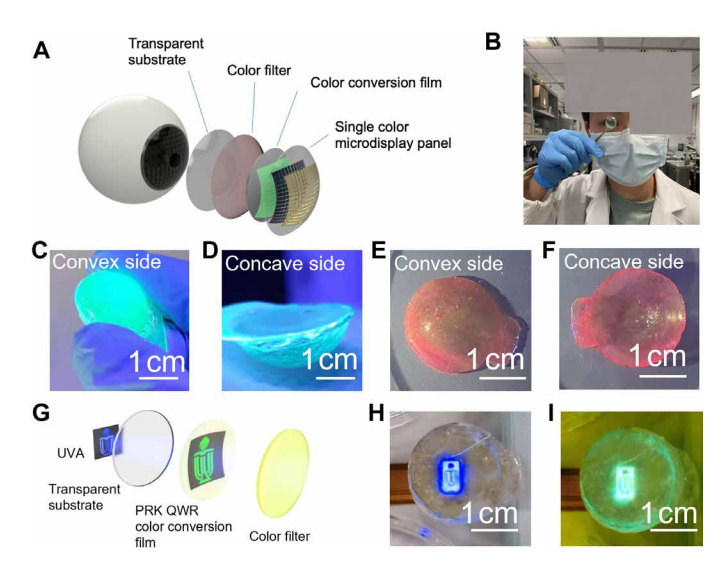


Fig. 6. Hemispherical color conversion film for potential contact lens microdisplay application. (A) Diagram showing the concept of the color conversion film for contact lens microdisplay. (B) A prototype hemispherical film with potential application as a contact lens. Note that the sample does not touch human eye and is just for concept proof. (C) Convex side and (D) concave side of the green perovskite quantum wire–based color conversion film. (E) Convex side and (F) concave side of the red perovskite quantum wire–based color conversion film. (G) Diagram showing the testing setup: UVA display panel/hemispherical transparent substrate/hemispherical color conversion film/color filter. (H) Optical photo of a working UVA/hemispherical color conversion film architecture. (I) Optical photo of a working UVA/hemispherical color conversion film/color filter architecture.

flat, micro/nanolens are needed for focusing. As for the hemispherical display, lenses can be avoided.

Regarding the thickness of the prototype contact lens color conversion film, flexible contact lenses usually have a thickness of 50 to 150 μ m, while rigid lenses usually have a thickness of ~200 μ m. According to our optical simulations (table S3), when the film

thickness increases to 8 μ m, the blue leakage will be reduced to only 2.4%, making a color filter unnecessary. Without the color filter, the total thickness can be controlled to ~8 μ m, much thinner than that of conventional contact lens.

DISCUSSION

Here, the EBL method is used to demonstrate the capability of feature size downscaling. However, in practical applications, photolithography with high resolution or nanoimprinting with high throughput can be used to meet the potential demands of upscaling. With nanoimprint lithography, submicrometer patterns can be achieved at wafer scale (22). We also explore lithography on curved surface; the results and related discussion can be found in figs. S9 and S10.

Figure 5F presents the pattern of circular arrays with a 400-nm pitch and a 180-nm opening diameter. This serves as a direct and compelling demonstration of our minimum feature size and maximum pixel density. However, because of the limitations of our experimental equipment, it is extremely challenging to directly observe the PL of perovskite pixel arrays with these small feature sizes. In addition, identifying the original openings in the PMMA for perovskite crystals after high-temperature growth is challenging, as the PMMA is damaged during the growth process, which makes direct observation challenging. We have attempted to address this issue using the near-field scanning optical microscope (NSOM) method, but the limited height range of the NSOM probe prevents it from effectively scanning our PMMA or perovskite patterns. In future work, we aim to optimize our samples and equipment further to enable direct observation of perovskite patterns with feature sizes of 180 nm or smaller.

In conclusion, we have fabricated ultrahigh–pixel density perovskite quantum wire arrays by the unique sa-CSS growth method, which is compatible with high-resolution wet lithography approaches. To demonstrate their potential for microdisplay, we have fabricated red, green, and blue color conversion devices with a minimum pixel size of 0.18 μm and a pitch size of 400 nm, corresponding to a pixel density of 63,500 ppi, which is currently the highest density achieved

for perovskite materials. We have also demonstrated a proof-of-concept contact lens display device on nonplanar substrates. These results indicate the great potential of perovskite quantum wire arrays and the pixelation strategy in high-density displays, image sensing, memristor arrays, nanophotonic circuitry, and other large-scale integrated optoelectronic devices.

MATERIALS AND METHODS

Chemicals

CsBr, PbBr₂, cesium iodide (CsI), cesium chloride (CsCl), phenethylammonium bromide (PEABr), lead iodide (PbI₂), and dimethyl sulfoxide (DMSO) are purchased from Sigma-Aldrich. All chemicals are used as received without further purification.

PAM fabrication

Anodic anodization is performed with a power source providing different voltages for different pore geometries. A total of 5% $\rm H_2SO_4$ is used for 5-V anodization, generating a pore size of ~5.7 nm. For 200-nm-thick Al, it takes about 40 min to fully anodize the Al to be transparent.

Perovskite powder for green color conversion film

CsPbBr₃ powder for CSS growth is made by mixing CsBr and PbBr₂ powder (molar ratio CsBr:PbBr₂ = 3:1), grinding the powder thoroughly, and annealing the powder at 430°C in the air for 1 hour.

Red color conversion film

The red color conversion film is produced using a red perovskite precursor solution, which is made by mixing CsI, CsCl, PEABr, and PbI₂ in specific molar ratios (CsI:CsCl:PEABr:PbI₂ = 0.9:0.05:0.2:1) dissolved in DMSO at a concentration of 0.1 M. The solution is rotated at 60°C for ~2 hours before use. A 20-µl solution is dropped onto FTO/PAM, followed by spin coating at 3000 rpm. The sample is then annealed at 60°C for 20 min in a glove box filled with nitrogen after spin coating.

PL characterization

PL is measured with an Edinburgh FS5 PL system. The light source is a xenon lamp.

Photolithography process

Photolithography process uses the Karl Suss MA6 mask aligner. A layer of positive photo-resist (PR) (HPR 504) with a thickness range of 1.0 to 1.8 μm and a sensitive wavelength of 365 to 436 nm is spin-coated at 4000 rpm on top of the PAM. Before the exposure, the sample is soft baked at 110°C for 1 min. The exposure is conducted with an energy dose of 25 mW/cm² for 4.8 s, using a soda-lime glass/chromium (Cr) photomask made by laser direct writing. Subsequently, the PR is developed with the FHD-5 developer [1.3 to 3.3% Tetramethylammonium hydroxide (TMAH)] for 1 min.

RIE process

RIE process is performed with the GaN etcher. The radio frequency power is 500 W. The BCl₃ flow is 30 standard cubic centimeter per minute (SCCM) and the He flow is 15 SCCM. The etch rate is about 25 nm/min for PAM.

EBL process

EBL process is carried out with the Raith e-LiNE. A layer of PMMA is spin-coated on top of the PAM at 3000 rpm for 60 s, giving a thickness of about 150 nm. The sample is then baked at 180° C for 2 min. The exposure is carried out with the beam voltage of 10 keV. After that, the PMMA is developed with the developer [Methyl Isobutyl Ketone (MIBK):isopropyl alcohol (IPA) = 1:3] for 30 s. A layer of 100-nm-thick Ni is thermally evaporated on the sample. The lift-off process is completed with the mixture of acetone:IPA = 1:1 for 5 min.

PAM pore shrinking process

 Al_2O_3 ALD is done by depositing O_3 and trimethylaluminum alternatively. The detailed condition can be found in table S1. Each cycle of ALD gives ~0.08-nm Al_2O_3 (23). The chamber temperature is 200°C.

Hemispherical color conversion film

The hemispherical color conversion film fabrication process starts with deforming the Al sheet to obtain a hemispherical Al shell with the method described in our previous work (1), followed by Al anodization in 5 wt % H₂SO₄ solution with ~5-V voltage for 60 min. For the green perovskite quantum wire–based color conversion film, the CSS growth is carried out under the condition mentioned before. For the red perovskite quantum wire–based color conversion film, the hemispherical shell is fixed on glass and undergoes the spin coating and annealing process. After that, the perovskite quantum wire–based color conversion film is covered with a crystal bond and etched in mercury chloride (HgCl₂) in an IPA solution to remove the aluminum and get the hemispherical semitransparent color conversion film. The crystal bond can be removed by acetone etching (before perovskite quantum wire growth) to obtain the contact lens shape freestanding hemispherical film.

First-principles simulation

The density functional theory calculations were performed by using the Cambridge Sequential Total Energy Package. The generalized gradient approximation of the Perdew-Burke-Ernzerhof function was used in this investigation. The electron wave function is expanded by a plane wave basis with a kinetic energy cutoff of 500 eV. The K-point mesh is set to $1 \times 1 \times 1$. The periodic images were separated by a vacuum layer of 10~Å to eliminate image interactions.

Model description

On the basis of the (001) surface of Al_2O_3 , we expanded the cell by 4×4 to simulate the surface of Al_2O_3 . Subsequently, we constructed adsorption models for six different sites including Pb—O, and performed structural optimization with an energy tolerance of 2×10^{-5} eV per atom and a force tolerance of 0.05 eV/Å. On the basis of the optimized structures, we calculated their energies, the results of which are shown in the inset table of Fig. 2A.

Molecular dynamics method simulation

We used the molecular dynamics method using the LAMMPS software based on the LJ approach, Eq. 2, to simulate the adsorption and growth processes of CsPbBr $_3$ in porous Al $_2$ O $_3$ at conditions of 400°C and 1 Pa. The LJ interaction parameters for each atom are listed in table S4.

The equation for LJ potential is as follows:

$$E = 4\epsilon \left[\left(\frac{\sigma}{r} \right)^{12} - \left(\frac{\sigma}{r} \right)^{6} \right]$$
 (2)

Here, ϵ represents the coefficient of force intensity, σ is the bond length, and r is the distance between two atoms.

Supplementary Materials

This PDF file includes: Supplementary Text Figs. S1 to S16 Tables S1 to S4

REFERENCES AND NOTES

- L. Gu, S. Poddar, Y. Lin, Z. Long, D. Zhang, Q. Zhang, L. Shu, X. Qiu, M. Kam, A. Javey, Z. Fan, A biomimetic eye with a hemispherical perovskite nanowire array retina. *Nature* 581, 278–282 (2020).
- W.-T. Wang, P. Holzhey, N. Zhou, Q. Zhang, S. Zhou, E. A. Duijnstee, K. J. Rietwyk, J.-Y. Lin, Y. Mu, Y. Zhang, U. Bach, C.-G. Wu, H. L. Yip, H. J. Snaith, S.-P. Feng, Water- and heatactivated dynamic passivation for perovskite photovoltaics. *Nature* 632, 294–300 (2024).
- Y. Zhou, Z. Sun, Y. Ding, Z. Yuan, X. Qiu, Y. B. Cao, Z. Wan, Z. Long, S. Poddar, S. Kumar, W. Ye, C. L. J. Chan, D. Zhang, B. Ren, Q. Zhang, H.-S. Kwok, M. G. Li, Z. Fan, An ultrawide field-of-view pinhole compound eye using hemispherical nanowire array for robot vision. Sci. Robot. 9, eadi8666 (2024).
- Q. Zhang, M. M. Tavakoli, L. Gu, D. Zhang, L. Tang, Y. Gao, J. Guo, Y. Lin, S.-F. Leung, S. Poddar, Y. Fu, Z. Fan, Efficient metal halide perovskite light-emitting diodes with significantly improved light extraction on nanophotonic substrates. *Nat. Commun.* 10, 727 (2019).
- N. P. Gallop, D. R. Maslennikov, N. Mondal, K. P. Goetz, Z. Dai, A. M. Schankler, W. Sung, S. Nihonyanagi, T. Tahara, M. I. Bodnarchuk, M. V. Kovalenko, Y. Vaynzof, A. M. Rappe, A. A. Bakulin, Ultrafast vibrational control of organohalide perovskite optoelectronic devices using vibrationally promoted electronic resonance. *Nat. Mater.* 23, 88–94 (2024).
- J. Zhao, L.-W. Lo, Z. Yu, C. Wang, Handwriting of perovskite optoelectronic devices on diverse substrates. *Nat. Photonics* 17, 964–971 (2023).
- Y. Liu, F. Feng, K. Zhang, F. Jiang, K.-W. Chan, H.-S. Kwok, Z. Liu, Analysis of size dependence and the behavior under ultrahigh current density injection condition of GaN-based micro-LEDs with pixel size down to 3 μm. J. Phys. D Appl. Phys. 55, 315107 (2022).
- C. Zou, C. Chang, D. Sun, K. F. Böhringer, L. Y. Lin, Photolithographic patterning of perovskite thin films for multicolor display applications. *Nano Lett.* 20, 3710–3717 (2020).
- P. Zhang, G. Yang, F. Li, J. Shi, H. Zhong, Direct in situ photolithography of perovskite quantum dots based on photocatalysis of lead bromide complexes. *Nat. Commun.* 13, 6713 (2022).
- Y. Zou, L. Cai, T. Song, B. Sun, Recent progress on patterning strategies for perovskite light-emitting diodes toward a full-color display prototype. Small Sci. 1, 2000050 (2021).
- K. Sun, D. Tan, X. Fang, X. Xia, D. Lin, J. Song, Y. Lin, Z. Liu, M. Gu, Y. Yue, J. Qiu, Threedimensional direct lithography of stable perovskite nanocrystals in glass. Science 375, 307–310 (2022).
- Y. Duan, R. Yu, H. Zhang, W. Yang, W. Xie, Y. Huang, Z. Yin, Programmable, high-resolution printing of spatially graded perovskites for multispectral photodetectors. *Adv. Mater.* 36, e2313946 (2024).
- G. H. Lee, K. Kim, Y. Kim, J. Yang, M. K. Choi, Recent advances in patterning strategies for full-color perovskite light-emitting diodes. *Nano Micro Lett.* 16, 45 (2023).
- J. Zhang, J. Lei, W. Xie, Z. Fang, Y. Li, Q. Du, SuperYOLO: Super resolution assisted object detection in multimodal remote sensing imagery. *IEEE Trans. Geosci. Remote Sens.* 61, 5605415 (2023).
- W. J. Baek, J. Park, J. Shim, B. H. Kim, S. Park, H. S. Kim, D.-M. Geum, S. H. Kim, Ultra-lowcurrent driven InGaN blue micro light-emitting diodes for electrically efficient and self-heating relaxed microdisplay. *Nat. Commun.* 14, 1386 (2023).
- L. Qi, X. Zhang, W. C. Chong, K. M. Lau, Monolithically integrated high-resolution full-color GaN-on-Si micro-LED microdisplay. *Photonics Res.* 11, 109–120 (2023).
- C. Xiang, J. Liu, J. Guo, L. Chang, R. N. Wang, W. Weng, J. Peters, W. Xie, Z. Zhang, J. Riemensberger, J. Selvidge, T. J. Kippenberg, J. E. Bowers, Laser soliton microcombs heterogeneously integrated on silicon. *Science* 373, 99–103 (2021).
- D. Zhang, Q. Zhang, B. Ren, Y. Zhu, M. Abdellah, Y. Fu, B. Cao, C. Wang, L. Gu, Y. Ding, K.-H. Tsui, S. Fan, S. Poddar, L. Shu, Y. Zhang, D.-B. Kuang, J.-F. Liao, Y. Lu, K. Zheng, Z. He, Z. Fan, Large-scale planar and spherical light-emitting diodes based on arrays of perovskite quantum wires. *Nat. Photonics* 16, 284–290 (2022).

- D. Lee, S. Cho, C. Park, K. R. Park, J. Lee, J. Nam, K. Ahn, C. Park, K. Jeon, H. Yuh, W. Choi, C. H. Lim, T. Kwon, Y. H. Min, M. Joo, Y.-H. Choi, J. S. Lee, C. Kim, S. Kwon, Fluidic self-assembly for microLED displays by controlled viscosity. *Nature* 619, 755–760 (2023).
- Y. Fu, S. Poddar, B. Ren, Y. Xie, Q. Zhang, D. Zhang, B. Cao, Y. Tang, Y. Ding, X. Qiu, L. Shu, J.-F. Liao, D.-B. Kuang, Z. Fan, Strongly quantum-confined perovskite nanowire arrays for color-tunable blue-light-emitting diodes. ACS Nano 16, 8388–8398 (2022).
- D. Zhang, L. Gu, Q. Zhang, Y. Lin, D.-H. Lien, M. Kam, S. Poddar, E. C. Garnett, A. Javey,
 Fan, Increasing photoluminescence quantum yield by nanophotonic design of quantum-confined halide perovskite nanowire arrays. Nano Lett. 19, 2850–2857 (2019).
- Z. Fan, J. C. Ho, Z. A. Jacobson, R. Yerushalmi, R. L. Alley, H. Razavi, A. Javey, Wafer-scale assembly of highly ordered semiconductor nanowire arrays by contact printing. *Nano Lett.* 8, 20–25 (2008).
- M. Groner, F. Fabreguette, J. Elam, S. George, Low-temperature Al₂O₃ atomic layer deposition. Chem. Mater. 16, 639–645 (2004).
- M. Hu, Y. Wang, S. Hu, Z. Wang, B. Du, Y. Peng, J. Yang, Y. Shi, D. Chen, X. Chen, Z. Zhuang, Z. Wang, X. Chen, J. Yang, Y. Ge, E. Wang, Q. Wen, S. Xiao, M. Ma, W. Li, J. Zhang, D. Ning, L. Wei, C. Yang, M. Chen, A pixelated liquid perovskite array for high-sensitivity and high-resolution x-ray imaging scintillation screens. Nanoscale 15, 15635–15642 (2023).
- A. Morozov, P. Gostishchev, A. Zharkova, A. Vasilev, A. Aleksandrov, L. Luchnikov, A. Tameev, D. Kiselev, T. Ilina, A. Ishteev, S. I. Didenko, D. S. Saranin, Micro-pixelated halide perovskite photodiodes fabricated with ultraviolet laser scribing. *Appl. Phys. Lett.* 124, 223503 (2024).
- G.-H. Dun, H. Zhang, K. Qin, X. Tan, R. Zhao, M. Chen, Y. Huang, X.-S. Geng, Y.-Y. Li, Y. Li, P. Wan, G.-Y. Gou, Q.-X. Feng, X.-R. Zheng, R. Liang, D. Xie, Y. Zhou, X. Wang, H. Tian, Y. Yang, T.-L. Ren, Wafer-scale photolithography-pixeled Pb-free perovskite x-ray detectors.
 ACS Nano 16, 10199–10208 (2022).
- C. Li, X. Ye, J. Jiang, Q. Guo, X. Zheng, Q. Lin, C. Ge, S. Wang, J. Chen, Z. Gao, G. Zhang, X. Tao, Y. Liu, High-throughput growth of armored perovskite single crystal fibers for pixelated arrays. Small 20, e2401624 (2024).
- S. Tian, F. Sui, K. He, G. Cheng, Y. Ge, D. Ning, Z. Wang, Z. Wang, G. Tao, Z. Wang, B. Du, L. Wei, W. Li, C. Yang, M. Chen, Co-axial silicon/perovskite heterojunction arrays for high-performance direct-conversion pixelated x-ray detectors. *Nano Energy* 78, 105335 (2020).
- C. Huang, Y. Chen, X.-L. Wang, B. Zhu, W.-J. Liu, S.-J. Ding, X. Wu, Flexible microspectrometers based on printed perovskite pixels with graded bandgaps. ACS Appl. Mater. Interfaces 15, 7129–7136 (2023).

Acknowledgments: We would like to express our gratitude to Z. Zheng and X. Zhang from the Department of ECE at HKUST for professional discussions on pixelation and microdisplays. We also thank K. Zhang and Z. Liu from SUSTech, Shenzhen for valuable technical input. In addition, we extend thanks to C. Zhou, Z. Jin, and J. Wang from the Department of Physics at HKUST for technical assistance. We thank technical support from Materials Characterization & Preparation Facility (CWB) and Nanosystem Fabrication Facility (CWB), HKUST. We also receive the support from State Key Laboratory of Advanced Displays and Optoelectronics Technologies, HKUST. The display panel used was purchased from Shenzhen Sitan Technology Ltd. Z.F. acknowledges the support from the New Cornerstone Science Foundation through the XPLORER PRIZE and Hong Kong Alliance of Technology and Innovation through BOCHK Science and Technology Innovation Prize. Funding: This work was supported by Hong Kong Research Grant Council, General Research Fund, 16205321 and 16214619 (to Z.F.); NSFC-RGC, Joint Research Fund, N_HKUST657/22 (to Z.F.); Guangdong-Hong Kong-Macao Intelligent Micro-Nano Optoelectronic Technology Joint Laboratory, Laboratory Funding, 2020B1212030010 (to Z.F.); National Key Research and Development Program of China, 2023YFC2505900 (to X.M.); and State Key Laboratory of Photovoltaic Science and Technology, 202401030303 (to O.Z. and X.M.). Author contributions: Conceptualization: O.Z., X.S., G.C. H.L., X.M., and Z.F. Methodology: Q.Z., X.S., G.C., Z.M., D.Z., Y.Z., X.Q., H.L., X.M., and Z.F. Investigation: Q.Z., X.S., G.C., Z.M., D.Z., Y.Z., W.T., H.L., X.M., and Z.F. Visualization: Q.Z., G.C., Z.M., Y.D., and H.L. Supervision: Q.Z., H.L., X.M., and Z.F. Writing—original draft: Q.Z., X.S., S.P., H.L., and Z.F. Writing—review and editing: Q.Z., Z.M., D.Z., X.Q., S.P., H.L., X.M., Z.F., and X.S. Funding acquisition: Q.Z., H.L., X.M., and Z.F. Data curation: Q.Z., G.C., Z.M., H.L., X.M., and Z.F. Formal analysis: Q.Z., G.C., X.Q., W.T., H.L., and Z.F. Software: Q.Z., G.C., and H.L. Project administration: O.Z., S.P. H.L., X.M., and Z.F. Validation: O.Z., X.S., G.C., Z.M., X.M., and Z.F. Resources: O.Z., B.R., X.M., and Z.F. Competing interests: The authors declare that they have no competing interests. Data and materials availability: All data needed to evaluate the conclusions in the paper are present in the paper and/or the Supplementary Materials.

Submitted 5 November 2024 Accepted 9 April 2025 Published 14 May 2025 10.1126/sciadv.adu3840